



This is a repository copy of *Towards quantification of doping in gallium arsenide nanostructures by low-energy scanning electron microscopy and conductive atomic force microscopy*.

White Rose Research Online URL for this paper:

<https://eprints.whiterose.ac.uk/207988/>

Version: Published Version

Article:

Guo, R. and Walther, T. orcid.org/0000-0003-3571-6263 (2024) Towards quantification of doping in gallium arsenide nanostructures by low-energy scanning electron microscopy and conductive atomic force microscopy. *Journal of Microscopy*, 293 (3). pp. 160-168. ISSN 0022-2720

<https://doi.org/10.1111/jmi.13263>

Reuse

This article is distributed under the terms of the Creative Commons Attribution (CC BY) licence. This licence allows you to distribute, remix, tweak, and build upon the work, even commercially, as long as you credit the authors for the original work. More information and the full terms of the licence here:

<https://creativecommons.org/licenses/>

Takedown

If you consider content in White Rose Research Online to be in breach of UK law, please notify us by emailing eprints@whiterose.ac.uk including the URL of the record and the reason for the withdrawal request.



eprints@whiterose.ac.uk
<https://eprints.whiterose.ac.uk/>

Towards quantification of doping in gallium arsenide nanostructures by low-energy scanning electron microscopy and conductive atomic force microscopy

Ran Guo | Thomas Walther 

Department of Electronic & Electrical Engineering, University of Sheffield, Sheffield, UK

Correspondence

Thomas Walther, Department of Electronic & Electrical Engineering, University of Sheffield, Mappin Building, Mappin Street, Sheffield S1 3JD, UK.
Email: t.walther@sheffield.ac.uk

Abstract

We calculate a universal shift in work function of 59.4 meV per decade of dopant concentration change that applies to all doped semiconductors and from this use Monte Carlo simulations to simulate the resulting change in secondary electron yield for doped GaAs. We then compare experimental images of doped GaAs layers from scanning electron microscopy and conductive atomic force microscopy. Kelvin probe force microscopy allows to directly measure and map local work function changes, but values measured are often smaller, typically only around half, of what theory predicts for perfectly clean surfaces.

KEYWORDS

atomic force microscopy (AFM), doping, GaAs, Kelvin probe force microscopy (KPFM), scanning electron microscopy (SEM)

1 | INTRODUCTION

Doping is the intentional local change of the conductivity in semiconductors by adding impurity atoms and as such this bandgap engineering forms the basis for all *pn*-junctions found in diodes and many field-effect transistors. There have been numerous studies of secondary electron (SE) imaging in scanning electron microscopy (SEM) of doped semiconductor layers, mostly in Si^{1–13} but also a few for SiC,¹⁴ InP,^{15–17} GaAs^{18–20} and, most recently, GaN.²¹ The central problem here has always been to predict and interpret correctly the image contrast, though it was recognised right from the beginning²² that under most imaging conditions *p*-type layers appear bright¹⁸ and *n*-type dark,¹⁹ for which the origin of the secondary electron emission from doped regions needed to be understood. As the escape depth for secondary electrons is only a few nanometres,

the quality and cleanliness of the surfaces (oxidation, carbon contamination, passivation by chemical treatments) and subsurfaces (disordering or amorphisation by ion implantation) is paramount and must be investigated in a reproducible manner, which the above studies on silicon have already started to address.

2 | THEORY

2.1 | Universal work function shift

The Fermi level in a doped semiconductor lies between the highest energy level E_v in the valence band and the lowest energy level E_c in the conduction band, roughly in the centre of the bandgap for intrinsic or very low doping levels. Its dependence on temperature T and doping levels can be

This is an open access article under the terms of the [Creative Commons Attribution](https://creativecommons.org/licenses/by/4.0/) License, which permits use, distribution and reproduction in any medium, provided the original work is properly cited.

© 2024 The Authors. *Journal of Microscopy* published by John Wiley & Sons Ltd on behalf of Royal Microscopical Society.

described by the following relationship if all dopants are ionised²³:

$$E_F = \frac{1}{2}(E_v + E_c) + \frac{3}{4}kT \ln \frac{m_p^*}{m_n^*} \pm kT \operatorname{arsinh} \frac{N_{D,A}}{2n_i}, \quad (1)$$

where k is the Boltzmann constant, T the absolute temperature, $m_{p,n}^*$ are the effective masses of holes and electrons respectively, n_i is the intrinsic charge carrier density, N_D the density of donor ions and N_A the density of acceptor ions. For n -doping N_D is used with the + sign, for p -doping N_A is used with the – sign in front of the inverse hyperbolic function.

The shift in Fermi level between two differently doped n -regions of the same material at the same temperature is thus

$$\Delta E_F = E_{F,1} - E_{F,2} = kT \operatorname{arsinh} \frac{N_{D,1}}{2n_i} - kT \operatorname{arsinh} \frac{N_{D,2}}{2n_i}, \quad (2)$$

where we can use the identity

$$\operatorname{arsinh} x = \ln \left(x + \sqrt{x^2 + 1} \right) \quad (3)$$

and the approximation

$$\operatorname{arsinh} x \approx \ln(2x) \quad (4)$$

for large values of $x = N_{D,A}/(2n_i)$, hence

$$\Delta E_F \approx kT \ln \frac{N_{D,1}}{n_i} - kT \ln \frac{N_{D,2}}{n_i} = kT \ln \frac{N_{D,1}}{N_{D,2}}. \quad (5)$$

For p -doping the equivalent term of $kT \ln \frac{N_{A,2}}{N_{A,1}}$ (with opposite sign) is obtained. For larger n -doping, the Fermi level shifts upwards within the bandgap of bulk material, for larger p -doping downwards. When two differently doped regions are brought into contact, then the Fermi levels equilibrate and the band-structures are adjusted so that the Fermi levels are equal on both sides, implying that the band-edges shift downwards in the n -region and upwards in the p -region. Hence, the shift of the work function, $e\phi$, is equal in size but opposite in direction to the shift of the Fermi levels in the bulk, that is, for two differently n -doped regions

$$e \Delta \phi = -\Delta E_F \approx kT \ln \frac{N_{D,2}}{N_{D,1}}, \quad (6)$$

so that the work function increases with n -doping and decreases with p -doping. This result is universal for all materials and means that if the active n [p]-doping is enhanced by exactly one order of magnitude (a decade, i.e.

$\frac{N_{D,2}}{N_{D,1}} = 10$) then the change in surface potential predicted is $\Delta \phi = 2.3kT/e = 59.4$ mV at room temperature. This holds for all kinds of doped semiconductors if the dopants are electrically active. If the work function is increased by n -doping, it will be harder for secondary electrons to leave the material, so SE intensity will be decreased; for p -doping the work function is lowered, SEs can easier escape from the surface and the SE intensity increases. This is the general origin of doping contrast in SE imaging, though there have been speculations that other effects such as charging, fringing fields etc.^{22,20,6,9} might also be relevant.

In the following section, we simulate the influence of the work function shift with doping on the SE yield of GaAs measured in SEM in Section 3.2, and in Section 3.3 we explore the direct measurement of work function shift by Kelvin probe force microscopy (KPFM) in an atomic force microscope (AFM). In principle, scanning capacitance microscopy (SCM) in an AFM could provide higher spatial resolution maps than KPFM, due to the smaller tip-sample distance, but quantification of the amplitude signal (i.e. converting measured capacitances into carrier concentrations) is quite complex and needs extensive modelling.^{24,25} The total capacitance measured is made up of contributions from the apex of the tip, the cone of the tip and the cantilever²⁵ (so the tip geometry must be accurately measured, e.g. by SEM imaging), the surface oxide layer (whose thickness and permittivity need to be estimated²⁴) and the semiconductor probed underneath (whose carrier concentration is to be calculated). This approach was therefore not followed for GaAs here.

2.2 | Monte Carlo simulations

CASINO v3.3 is a Monte Carlo simulation software²⁶ that models multiple elastic and inelastic electron scattering, down to a cut-off energy at 50 eV and allows SE and back-scattered electron (BSE) yields to be calculated for materials as function of their density ($\rho_{\text{GaAs}} = 5.32$ g/cm³), plasmon energy ($E_{p,\text{GaAs}} = 15.8$ eV) and work function, ϕ . So we have modelled the BSE yield and the SE yields for doped GaAs as a function of the shift of the work function from the value of $e\phi_{\text{GaAs,I}} = 4.69$ eV for intrinsic GaAs, using the above shift of the work function from Equation (6). While the BSE yield is independent of doping and reaches a wide plateau around 0.36–0.37 for energies between 0.6 and 3 keV, the SE yield varies significantly with doping, as shown in Figure 1, reaching values well above unity around primary electron energies of 0.15–0.2 keV. For these low energies, the SE/BSE ratio therefore peaks at about 9.2 for 0.15 keV, 6.6 for 0.2 keV and 4.6 for 0.3 keV.

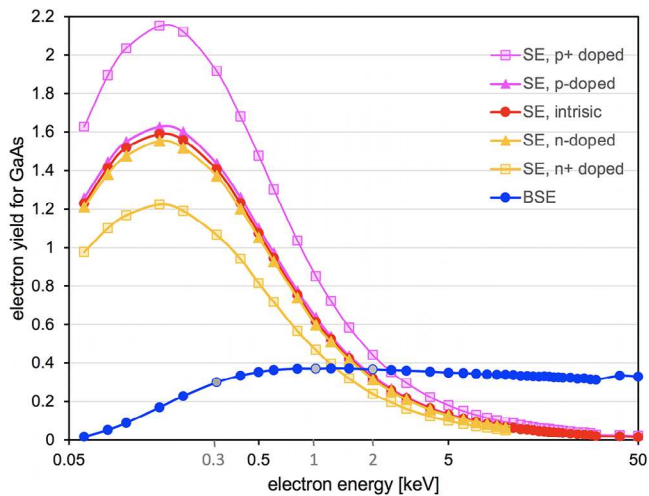


FIGURE 1 Monte Carlo simulation of BSE and ideal SE yield for GaAs versus acceleration voltage for different doping levels ($n_i = 2 \times 10^6 \text{ cm}^{-3}$, $n = p = 2 \times 10^7 \text{ cm}^{-3}$, $n^+ = p^+ = 2 \times 10^{18} \text{ cm}^{-3}$). BSE yield (blue) is unaffected by doping.

These simulations thus make the case for low-kV SEM operation in the range 0.15–0.5 keV where the SE yields are high and differ significantly as function of doping level, while the BSE yield is low (and hence generation of problematic SE2 and SE3 type electrons generated by BSEs from sample and vacuum chamber, respectively, would be minimal). There should thus be no need for energy filtering or biasing as a means of BSE suppression as has been previously suggested ought to be used for dopant mapping.^{1,11} The expected contrast from *p*-doping would be $+2.8 \pm 0.2\%$ per decade, the predicted contrast from *n*-doping is $-2.0 \pm 0.1\%$ per decade, over the range of acceleration voltages from 0.06 kV to 10 kV, so that full quantification may be possible for all doping levels.

Figure 2 displays a double-logarithmic plot of the maximum electron penetration depth versus primary electron energy. For energies ≤ 0.1 keV (red filled squares) the penetration depth is <1 nm and so the electrons will not be able to penetrate even very thin surface oxide or contamination layers. For energies of 0.12–0.15 keV (orange filled squares) the penetration depth is just 2–5 nm, which correlates well with the typical escape depths predicted for SEs in Si.^{9,12} For energies in the range of 1–2 keV (grey filled squares) as used in most studies in the literature and also in Figure 3 the penetration is already 20–55 nm, making the signal less surface sensitive but also degrading the lateral resolution by sideways straddling due to multiple scattering to widths of more than 10 nm. Energies in the range 0.3–0.5 keV (yellow filled squares) should form the best compromise, with maximum SE penetration of 5.5–8.5 nm, although 0.15–0.20 keV (orange filled squares) would have

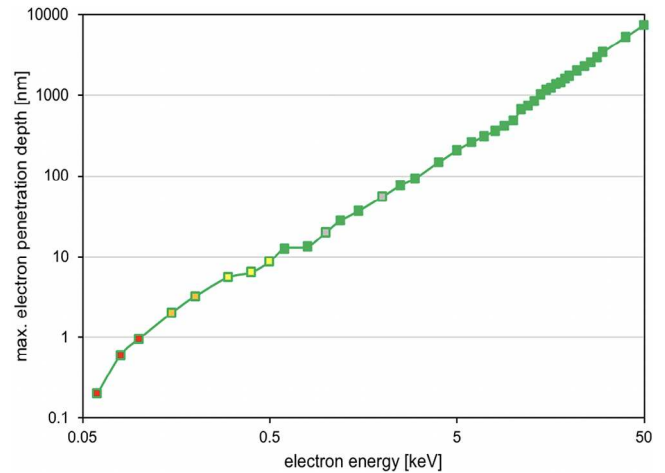


FIGURE 2 Plot of maximum electron penetration into GaAs versus acceleration voltage.

TABLE 1 Layer structures investigated.

Structure	Nominal thickness	<i>p</i> -doping	<i>n</i> -doping
Layer 3	200 nm	$1.6 \times 10^{19} \text{ cm}^{-3}$	$9.0 \times 10^{17} \text{ cm}^{-3}$
Layer 2	200 nm	$5.6 \times 10^{18} \text{ cm}^{-3}$	$1.2 \times 10^{18} \text{ cm}^{-3}$
Layer 1	200 nm	$2.8 \times 10^{18} \text{ cm}^{-3}$	$2.1 \times 10^{18} \text{ cm}^{-3}$
Buffer	500 nm (p) or 300 nm (n)	$1.0 \times 10^{18} \text{ cm}^{-3}$	$3.7 \times 10^{17} \text{ cm}^{-3}$
Substrate	350 μm	i	i

Note: Nominally undoped layers are listed as intrinsic (i).

given a slightly higher SE/BSE yield ratio according to Figure 1.

3 | EXPERIMENTAL SECTION

3.1 | Epitaxial growth

Two GaAs(001) wafers with doping staircases as listed in Table 1, one with three *p*-doped layers on a *p*-type buffer and one with three *n*-doped layers on an *n*-type buffer layer, were grown by molecular beam epitaxy in a VG V90 chamber and calibrated by electrical measurements in the National Epitaxy Facility at the University of Sheffield. Similar layers were used to fabricate efficient light emitting diodes. Be was used as *p*-dopant, Si as *n*-dopant. Wafer pieces were back-thinned to 100–200 μm thickness and then cleaved and stored in evacuated plastic containers with silica gel before being transferred to the microscopes to keep the native oxide as thin as possible (about 1–1.5 nm).^{27,28} During times of high humidity in the autumn and winter months, longer storage in air could lead to decomposition of the native oxide.

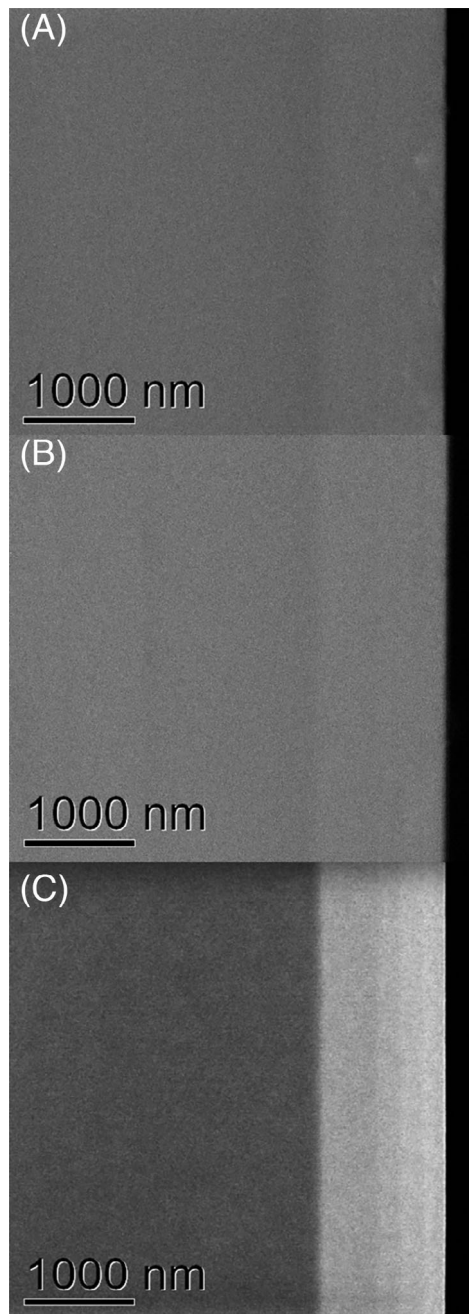


FIGURE 3 In-lens SE images recorded of Be-doped *p*-GaAs with different SEM instruments: Raith EO at 1 keV (A), Raith EO at 2 keV (B) and Hitachi Regulus 8100 at 1.5 keV and with +1.5 V on the signal electrode within the objective pole-piece, which eliminates BSEs and all SEs with energies below 1.5 eV, giving almost exclusive SE1 signals as modelled in Section 2.2. Sampling is 7.1 nm/pixel for (a, b) and 8.8 nm/pixel for (C). Growth direction is from left to right. *p*-Doped layers appear bright (positive contrast).

3.2 | Scanning electron microscopy

We have used various field-emission SEM instruments with in-lens detectors from different manufacturers and in the following report results only from two where clear

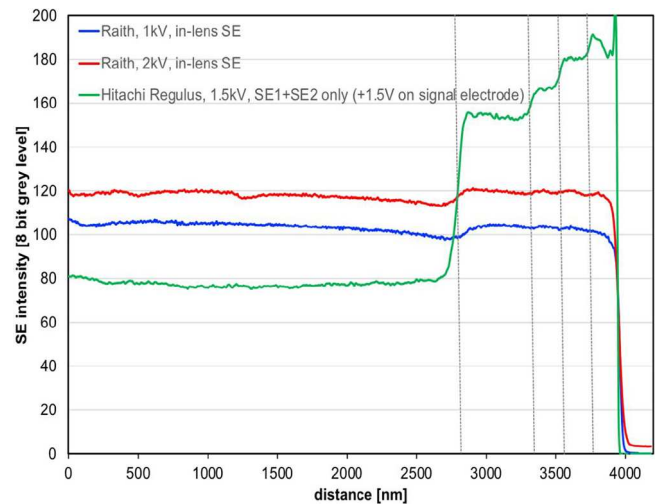


FIGURE 4 Line traces of vertically integrated SE intensities from Figure 3.

SE images of the doped layers could be obtained at 1–2 keV, using either Raith EO or Hitachi Regulus SEM instruments. The examples of in-lens SE images shown in Figure 3 and 4 illustrate that positive doping contrast can be obtained from *p*-doped GaAs but the image contrast is weak for 1–2 keV primary energies and depends heavily on the set-up of any small internal bias applied to electrodes within the objective lens pole-piece, making quantification very difficult and prone to errors. The dotted vertical lines in Figure 4 are the positions of the inflection points of the line traces, which correspond to the interfaces of the various layers in the doping staircase sample and allow the thicknesses of the lightly doped buffer layer (512 ± 18 nm instead of nominal 500 nm) and the three more heavily doped layers in the staircase sample (203 ± 11 nm instead of nominal 200 nm) to be measured with an accuracy limited by both the depletion width of the built-in potential of the *pn*-junctions^{10,12} and the effective SE resolution. The absolute intensities, however, cannot be easily interpreted: without any bias on the focusing electrodes, each of the top *p*-layers gives 3–4% contrast relative to the layer directly beneath, with bias on the focusing electrodes the contrast is much higher than our simulations predict.

Doping contrast from *n*-doped GaAs has been much harder to obtain, for three reasons: first, because the doping staircase in this case has an inverted order, having the highest doped layer grown first and then layers of reduced doping levels nearer the surface; second, because the experimental doping levels in the layers are slightly lower (cf. Table 1) and, third, Figure 1 indicates that SE1 contrast for *n*-doping is actually a little smaller than for the same levels of *p*-doping if the doping levels are high, because the same shifts of work function lead to slightly asymmetric effects on the SE yield, which has not been

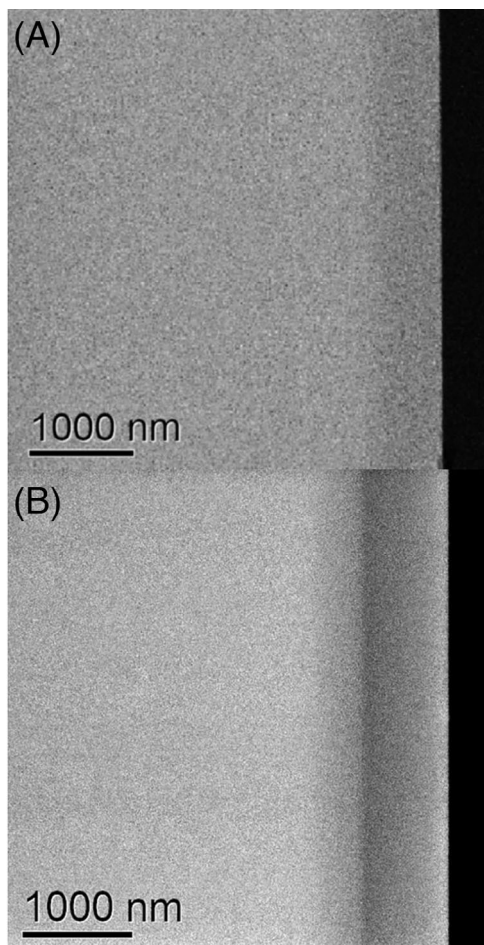


FIGURE 5 In-lens SE images of Si-doped *n*-GaAs recorded with different SEM instruments: Raith EO at 1 keV, 4.5 nm/pixel (A) and Hitachi Regulus 8100 at 1 keV, 5.78 nm/pixel (B). Layers are barely visible and appear dark (negative contrast).

reported in the literature so far, the shift upwards for *p*-type being slightly stronger than the corresponding shift downwards for *n*-type.

So far, we have not been able to perform useful experiments at acceleration voltages lower than 1 kV because the chromatic probe spread in our SEM instruments prevented us to obtain meaningful data. As the resolution due to chromatic aberration is generally given by²⁹

$$d_c = C_c \beta \Delta E / (eU), \quad (7)$$

work at low voltages *U* will necessitate at least one of the following modifications to a standard SEM instrument, because for typical values of $C_c = 8 \text{ mm}$, $\beta = 0.01$, $\Delta E = 0.8 \text{ eV}$, $U = 300 \text{ V}$, the chromatic broadening would be much larger than our thinnest layers are wide (200 nm):

- i. inclusion of a chromatic aberration corrector to reduce the aberration constant C_c ,
- ii. inclusion of a monochromator to reduce the primary energy width ΔE of the probe,

- iii. inclusion of a tiny condenser aperture to bring the beam convergence angle β close to the diffraction limit ($\approx 1.5 \text{ mrad}$ would be needed at $U = 0.3 \text{ kV}$).

This has not been possible so far; however, work along point iii is planned by the corresponding author as being a much cheaper option than would be following routes i or ii.

3.3 | Atomic force microscopy

The CSI Nano-Observer is a versatile atomic force microscope and has been used at the manufacturer site in Les Ulis near Paris, France, to study the *p*-doped sample as described below. Using a metal-coated sharp conductive tip, the AFM can be used to measure the current between the tip for constant bias and then directly calculate the resistance from Ohm's law. The key problem in this type of contact-mode conductive AFM (c-AFM) is that the resistance and hence the current can rapidly change over many orders of magnitude when the tip is scanned over a semiconducting surface, so the current detecting operational amplifier must be able to adjust its transimpedance very quickly. For a doping staircase in silicon this and microwave reflectivity measurements have directly allowed mapping of the resistivity, capacitance and doping density of several μm wide layers.³⁰

Another possibility of electrical measurements is presented by tapping-mode electrical force measurements called Kelvin probe force microscopy (KPFM) where the oscillating tip and the sample form a capacitor that stores an amount of electric energy given by

$$W = \frac{1}{2} CV_{tip}^2, \quad (8)$$

where C is the local capacitance and

$$V_{tip} = V_{DC} - e \Delta\phi + V_{AC} \sin \omega t \quad (9)$$

is the voltage between tip and sample, which is given by the applied bias with DC and AC components and the surface potential ϕ . The electric force between tip and sample surface along the vertical direction z then is

$$F = -\frac{\partial W}{\partial z} = -\frac{1}{2} \frac{\partial C}{\partial z} V_{tip}^2 \quad (10)$$

and inserting Equation (9) into Equation (10) gives

$$F = -\frac{1}{2} \frac{\partial C}{\partial z} \left(V_{DC} - \frac{1}{2} V_{AC}^2 - e\phi \right)^2 - \frac{\partial C}{\partial z} (V_{DC} - e\phi) V_{AC} \sin \omega t + \frac{1}{4} \frac{\partial C}{\partial z} V_{AC}^2 \cos 2\omega t, \quad (11)$$

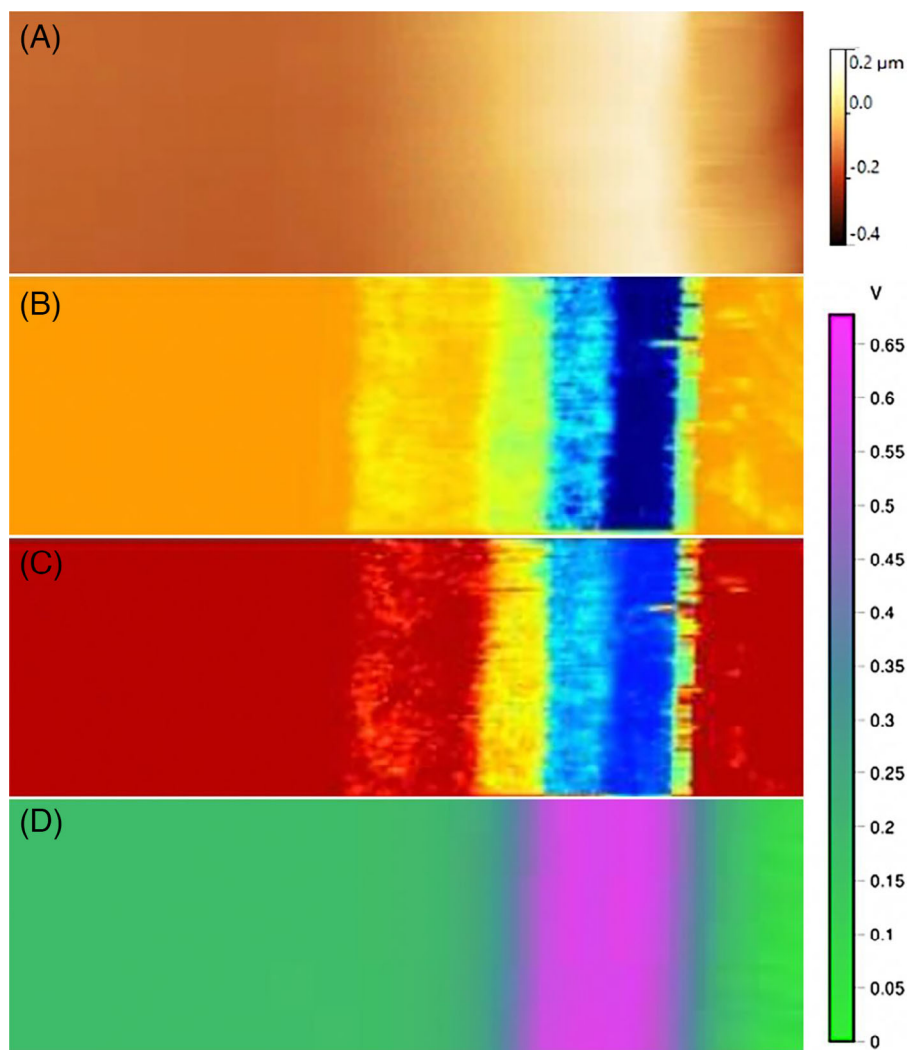


FIGURE 6 c-AFM of Be-doped p-GaAs with $2.6 \mu\text{m}$ long \times $0.8 \mu\text{m}$ wide maps of topography with height scale bar in sepia (A), current (B), resistance (C) and KPFM from another area of the same wafer, with green-purple scale bar of work function in volts (D). Growth direction is left to right, with the surface at $\approx 300 \text{ nm}$ from the right edge.

where the first term is a static component, the second an oscillation with base frequency ω and the third an oscillation with double frequency, 2ω . If the second term is nulled by feedback, then one gets directly $V_{\text{DC}} = e\phi$ from which the surface potential ϕ can be obtained. Figures 6–8 depict maps and profiles of topography, current, resistance and surface potential for the *p*-doped GaAs sample.

Figure 6A shows the cleaved surface is smooth but inclined at a tiny angle of $\approx 2^\circ$ to the horizontal. Figure 6B and C are false colour maps of current and resistance, respectively, line traces of which are plotted in Figure 7. The buffer and all three doped layers are well visible in Figures 6b and c and 7; the layer on top the highest doped layer (green in Figure 6B and C) varies in apparent width between a single pixel ($\approx 10 \text{ nm}$) and 60 nm and is presumably representing the AFM tip going first over the native oxide and then descending steeply over the wafer edge.

KPFM study of $10 \mu\text{m}$ wide *p*-Si layers after HF surface treatment⁷ only gave 30 meV surface potential shift for 10 times higher doping levels, which is exactly half the value expected from Section 2.1. Here, we observe a shift in Figure 8 of about 430 meV between the substrate and the top two layers (which themselves cannot be really distinguished in Figure 6D despite a factor of almost $3\times$ in their nominal doping levels). Based on the values in Table 1, $\Delta\phi$ should have given individual shifts of $0.74\text{--}0.77 \text{ V}$ in the highest doped layers compared to an intrinsic substrate, indicating the need for an external calibration of the doping in the top two *p*-layers and also an estimate of the doping level in the nominally undoped (intrinsic) substrate. The shift between the two top layers themselves should have been 29 mV while the $7\text{--}9 \text{ mV}$ measured are close to the experimental noise level. The overall widths of the interfaces in KPFM mode appear to be wider than in

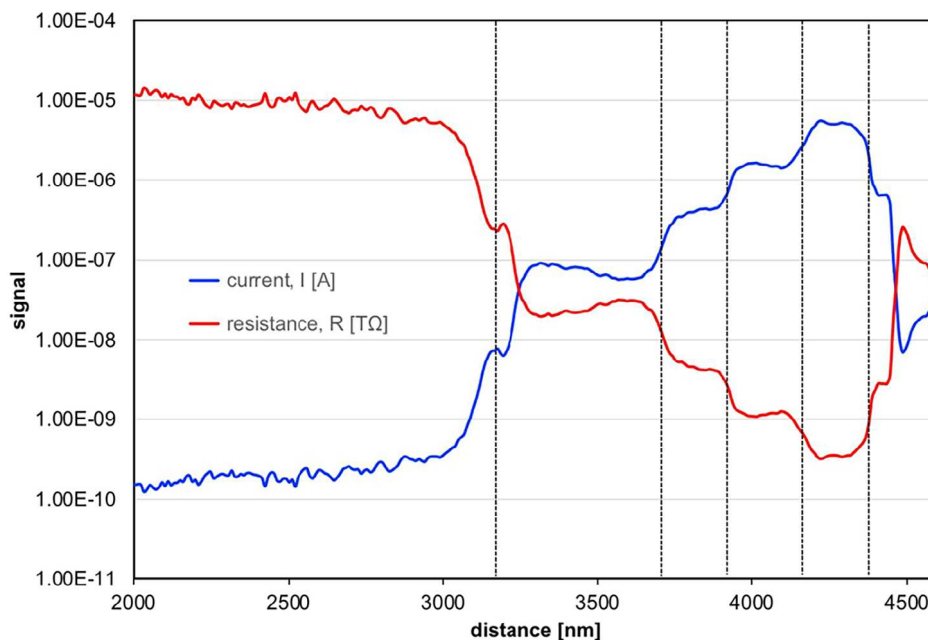


FIGURE 7 Vertically integrated line profiles of current (at constant bias of 1.8 V) and resistivity maps shown in Figures 6(B, C). The resistance lies in the MΩ to GΩ range so values have been divided by 10^{15} (i.e. plotted in units of $10^{15} \Omega = T\Omega$) to fit into the same range for display. Dotted lines again indicate inflection points. Sampling: 9.77 nm /pixel.

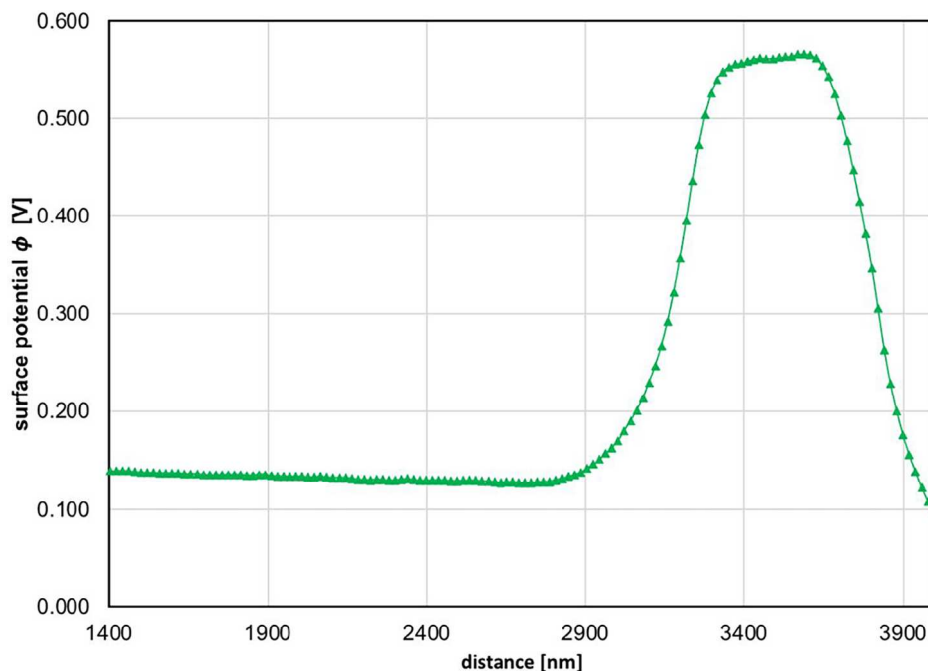


FIGURE 8 Line profile of surface potential map shown in Figure 6(D). Sampling: 19.5 nm/pixel.

the resistivity measurements, which can be explained by a decreased spatial resolution in tapping mode compared to contact mode. We estimate the effective spatial resolution in Figures 6D and 8 to lie in the range of 100–200 nm. No useful measurement of the *n*-doped wafer has been made by AFM, the corresponding samples having shown excessive dust from cleavage accumulating on a high number of cleavage steps.

4 | DISCUSSION AND CONCLUSION

An interpretation of the SE line traces in Figure 4 necessitates an extrapolation of intensity from the GaAs substrate region to the wafer edge to serve as reference, which needs to take into account the slight bending observed (convex for the Raith EO while slightly concave for the Hitachi Regulus). The SE intensity increase in % measured for buffers

TABLE 2 SE intensity analysis of *p*-type layers based on Figures 1 and 4.

Structure	Nominal <i>p</i> -doping (cm ⁻³)	Relative SE intensity increase (%)		Decades of doping increase		Measured <i>p</i> -doping (cm ⁻³)	
		Raith	Hitachi	Raith	Hitachi	Raith	Hitachi
Layer 3	1.6 × 10 ¹⁹	17 ± 4	148 ± 11	6.07	52.86	6.0 × 10 ¹⁹	–
Layer 2	5.6 × 10 ¹⁸	15 ± 2	134 ± 9	5.36	47.86	1.8 × 10 ¹⁹	–
Layer 1	2.8 × 10 ¹⁸	13 ± 2	117 ± 8	4.64	41.79	2.2 × 10 ¹⁸	4.4 × 10 ²²
Buffer	1.0 × 10 ¹⁸	12 ± 2	104 ± 8	4.29	37.14	Reference	
Substrate	i	Reference		–		Reference	

and thin layers relative to the nominally undoped substrate can then be calculated and quantified with the help of Figure 1 (2.8±0.2% increase of SE1 signal per decade increase of *p*-doping). Results are shown in Table 2. Herein, data for 1 and 2 kV from the Raith EO microscope have been combined, and for the final column the buffer layer has been used as reference because it was unclear whether the nominally undoped substrate would really have a carrier concentration as low as the intrinsic value of $n_i = 2 \times 10^6 \text{ cm}^{-3}$ tabulated for GaAs.

It is clear from Table 2 that the low-contrast SE images from the Raith EO microscope yield reasonable values that differ from the nominal ones by up to a factor of ×3.8, while the data from the Hitachi Regulus would give far too high values (for the two top layers these would actually lie above bulk density). A careful inspection of the raw image data shows that the SE intensity from the vacuum seems to have been clipped at zero where it may have gone negative otherwise, having cut-off a substantial background, which in turn led to an artificially high apparent contrast. It is also clear that for a variation of the nominal doping level by a factor of maximal ×16 between buffer and top layer, our simulations would have suggested to expect only a maximum contrast of 4.5% at 1–2 kV, which is lower than what has actually been measured by both instruments, indicating the need to expand the doping range for calibration of experimental contrast levels.

The low contrast from the *n*-doped GaAs even at 1 keV shown in Figure 5 may be due to a combination of the overall lower SE1 yield of *n*⁺-doped material (cf. Figure 1) as well as the relative high BSE yield which can generate additional SE2 proportional to the BSE yield and thus reduce contrast further.

Our simulations suggest that sub-kV imaging at about 0.3 kV using in-lens SE detectors may improve the SE1/BSE yield and thus the contrast in dopant mapping of semiconductors compared to the 1–5 kV primary SEM voltages typically being used at the present. 0.3 kV and 2.6 kV were identified earlier as the most suitable voltages to reduce charging in GaAs.³¹ Type-2 SEs (so-called SE2s that are produced by BSEs rather than directly by the primary

electrons) have been used in (4) to image highly doped layers but generally reduce image contrast. The angular collection range of the SE detector,³ trapped surface charges⁹ and various surface effects, such as carbonaceous overlayers,^{8,15} surface oxides,⁹ subsurface damage due to mechanical tripod polishing,^{5,14} chemical etching¹¹ and ion beam damage due to argon ion milling¹⁶ or focused Ga⁺ ion beam milling,¹³ have all been identified previously to reduce the contrast relative to the best surface preparation available, which is by cleavage. So doping mapping will only become fully quantitative and reproducible in different laboratories once one uses calibrated test structures and also defines standard operation procedures for specimen handling, where cleavage is the preferred option for sphalerite semiconductors as it yields the highest contrast.

ACKNOWLEDGEMENTS

The authors would like to thank a number of people: Ed Clarke and Shiyong Zhang from the National Epitaxy Facility at the University of Sheffield, for provision of the doped GaAs wafer samples; Steve Murray and Yukari Dan from Hitachi High-Tech Europe, Daresbury, for the SE images from the Hitachi Regulus 8100 SEM; Louis Pacheco and Emmanuel Lepleux from CSInstruments, Les Ulis, Paris, for provision of *c*-AFM and KPFM data.

ORCID

Thomas Walther  <https://orcid.org/0000-0003-3571-6263>

REFERENCES

- Schönjahn, C., Humphreys, C. J., & Glick, M. (2002). Energy-filtered imaging in a field-emission scanning electron microscope for dopant mapping in semiconductors. *Journal of Applied Physics*, 92(12), 7667–7671.
- Merli, P. G., Corticelli, F., & Morandi, V. (2002). Images of dopant profiles in low-energy scanning transmission electron microscopy. *Applied Physics Letters*, 81(24), 4535–4537.
- Schönjahn, C., Broom, R. F., Humphreys, C. J., Howie, A., & Mentink, S. A. M. (2003). Optimizing and quantifying dopant mapping using a scanning electron microscope with a through-the-lens detector. *Applied Physics Letters*, 83(2), 293–295.

4. Merli, P. G., Morandi, V., Savini, G., Ferroni, M., & Sberveglieri, G. (2005). Scanning electron microscopy of dopant distribution in semiconductors. *Applied Physics Letters*, *86*, 101916.
5. Kazemian, P., Twitchett, A. C., Humphreys, C. J., & Rodenburg, C. (2006). Site-specific dopant profiling in a scanning electron microscope using focused ion beam prepared specimens. *Applied Physics Letters*, *88*, 212110.
6. Walker, C. G. H., Zaggout, F., & El-Gomati, M. M. (2008). The role of oxygen in secondary electron contrast in doped semiconductors using low voltage scanning electron microscopy. *Journal of Applied Physics*, *104*, 123713.
7. Volotsenko, I., Molotskii, M., Barkay, Z., Marczewski, J., Grabiec, P., Jaroszewicz, B., Meshula, G., Grunbaum, E., & Rosenwaks, Y. (2010). Secondary electron doping contrast: Theory based on scanning electron microscopy and Kelvin probe force microscopy. *Journal of Applied Physics*, *107*, 014510.
8. Rodenburg, C., Jepson, M. A. E., Bosch, E. G. T., & Dapor, M. (2010). Energy selective scanning electron microscopy to reduce the effect of contamination layers on scanning electron microscope dopant mapping. *Ultramicroscopy*, *110*, 1185–1191.
9. Chee, A. K. W., Broom, R. F., Humphreys, C. J., & Bosch, E. G. T. (2011). A quantitative model for doping contrast in the scanning electron microscope using calculated potential distributions and Monte Carlo simulations. *Journal of Applied Physics*, *109*, 013109.
10. Jepson, M., Liu, X., Bell, D., Ferranti, D., Inkson, B., & Rodenburg, C. (2011). Resolution limits of secondary electron dopant contrast in helium ion and scanning electron microscopy. *Microscopy and Microanalysis*, *17*, 637–642.
11. Chee, A. K. W. (2016). Fermi level pinning characterisation on ammonium fluoride-treated surfaces of silicon by energy-filtered doping contrast in the scanning electron microscope. *Scientific Reports*, *6*, 32003.
12. Chee, A. K. W. (2016). Quantitative dopant profiling by energy filtering in the scanning electron microscope. *IEEE Transactions on Device and Materials Reliability*, *16*(20), 138–148.
13. Chee, A. K. W. (2020). Unravelling new principles of site-selective doping contrast in the dual-beam focused ion beam scanning electron microscope. *Ultramicroscopy*, *213*, 112947.
14. Buzzo, M., Leicht, M., Schweinböck, T., Ciappa, M., Stangoni, M., & Fichtner, W. (2004). 2D dopant profiling on 4H silicon carbide p⁺n junction by scanning capacitance and scanning electron microscopy. *Microelectronics and Reliability*, *44*, 1681–1686.
15. Tsurumi, D., Hamada, K., & Kawasaki, Y. (2010). Energy-filtered imaging in a scanning electron microscope for dopant contrast in InP. *Journal of Electron Microscopy*, *59*, S183–S187.
16. Tsurumi, D., & Hamada, K. (2013). Sensitive site-specific dopant mapping in scanning electron microscopy on specimens prepared by low energy Ar⁺ ion milling. *Applied Physics Express*, *6*, 126601.
17. Tsurumi, D., Hamada, K., & Kawasaki, Y. (2013). Observation of two-dimensional p-type dopant diffusion across a p⁺-InP/n⁻-InGaAs interface using scanning electron microscopy. *Journal of Applied Physics*, *113*, 144901.
18. Pavesi, L., Araujo, D., Ky, N. H., Garniere, J. D., Reinhard, F. K., & Buffat, P. A. (1991). Zinc diffusion in GaAs and zinc-induced disordering of GaAs/AlGaAs multiple quantum wells: a multitechnique study. *Optical and Quantum Electronics*, *23*, S789–S804.
19. Barkay, Z., Grunbaum, E., Shapira, V., Wilshaw, P., Barnham, K., Bushnell, D. B., Ekins-Daukes, N. J., & Mazzer, M. (2003). High-resolution scanning electron microscopy of dopants in p-i-n junctions with quantum wells. *Institute of Physics Conference Series*, *179*(2), 143–146.
20. Kaestner, B., Schönjahn, C., & Humphreys, C. J. (2004). Mapping the potential within a nanoscale undoped GaAs region using a scanning electron microscope. *Applied Physics Letters*, *84*(12), 2109–2111.
21. Zhang, K., Ban, C.-G., Yuan, Y., & Huang, L. (2023). Optimized dopant imaging for GaN by a scanning electron microscopy. *Journal of Microscopy*, *290*, <https://doi.org/10.1111/jmi.13206>
22. Perovic, D. D., Castell, M. R., Howie, A., Lavoie, C., Tiedje, T., & Cole, J. S. W. (1995). Field-emission SEM imaging of compositional and doping layer semiconductor superlattices. *Ultramicroscopy*, *58*, 104–113.
23. Arlt, G. (1985). *Werkstoffe der Elektrotechnik*. Lecture Script, RWTH Aachen, May, p. 268.
24. Williams, C. C. (1999). Two-dimensional dopant profiling by scanning capacitance microscopy. *Annual Review of Materials Science*, *29*, 471–504.
25. Colchero, J., Gil, A., & Baro, A. M. (2001). Resolution enhancement and improved data interpretation in electrostatic force microscopy. *Physical Review B*, *64*, 245403.
26. Hovington, P., Drouin, D., Gauvin, R., Joy, D. C., & Evans, N. (1997). CASINO: a new Monte Carlo code in C language for electron beam interactions – part III: stopping power at low energies. *Scanning*, *19*, 29–35.
27. Walther, T., Hetherington, C. J. D., & Humphreys, C. J. (1995). A contribution to the quantitative comparison of experimental high-resolution electron micrographs and image simulations. *Proc. Microscopy of Semiconducting Materials, Oxford. Inst. Phys. Conf. Ser.*, *146*, 53–56.
28. Walther, T., Humphreys, C. J., Grimshaw, M. P., & Churchill, A. C. (1995). Detection of random alloy fluctuations in high-resolution transmission electron micrographs of AlGaAs. *Philosophical Magazine A*, *72*, 1015–1030.
29. Walther, T., & Stegmann, H. (2006). Preliminary results from the first monochromated and aberration corrected 200-kV field-emission scanning transmission electron microscope. *Microscopy and Microanalysis*, *12*, 498–505.
30. Brinciotti, E., Gramse, G., Hommel, S., Schweinsboeck, T., Altes, A., Fenner, M. A., Smoliner, J., Kasper, M., Badino, G., Tuca, S.-S., & Kienberger, F. (2015). Probing resistivity and doping concentration of semiconductors at the nanoscale using scanning microwave microscopy. *Nanoscale*, *7*, 14715.
31. Joy, D. C. (1987). A model for calculating secondary and backscattered electron yields. *Journal of Microscopy*, *147*(1), 51–64.

How to cite this article: Guo, R., & Walther, T. (2024). Towards quantification of doping in gallium arsenide nanostructures by low-energy scanning electron microscopy and conductive atomic force microscopy. *Journal of Microscopy*, 1–9. <https://doi.org/10.1111/jmi.13263>